Cardiac Motion Estimation Using Covariant Derivatives and Helmholtz Decomposition

Alessandro Becciu[1], Remco Duits[1,2], Bart J. Janssen[2], Luc M.J. Florack[1,2], and Hans C. van Assen[1]

[1] Dept. of Biomedical Engineering, Eindhoven University of Technology, Netherlands
http://bmia.bmt.tue.nl
[2] Dept. of Mathematics, Eindhoven University of Technology, Netherlands

Abstract. Quantification of cardiac function is important for the assessment of abnormalities and response to therapy. We present a method to reconstruct dense cardiac motion from sparse features in tagging MRI, decomposed into solenoidal and irrotational parts using multi-scale Helmholtz decomposition. Reconstruction is based on energy minimization using covariant derivatives exploiting prior knowledge about the motion field. The method is tested on cardiac motion images. Experiments on phantom data show that both covariant derivatives and multi-scale Helmholtz decomposition improve motion field reconstruction.

Keywords: Cardiac function, MRI tagging, multi-scale, Helmholtz decomposition, covariant derivatives.

1 Introduction

MRI tagging admits detailed noninvasive intramural assessment of myocardial motion, quantification of which may help in (early) diagnosis of cardiac abnormalities such as ischemia and myocardial infarction.

Motion extraction may be based on the optic flow constraint equation (OFCE), originally developed for scalar images [1,2], which can be adapted to MRI tagging and extended to multiple scales [3]. Alternatively, feature tracking based on "demons" has been proposed in which certain features are preserved [4]. Multi-scale feature tracking with dense flow field reconstruction from a sparse set of anchor point velocities has been proposed for scalar sequences [5], but not for MRI tagging.

Kohlberger et al. [6] and Corpetti et al. [7] already exploited the Helmholtz decomposition to study the behavior of fluid flows. Cuzol et al. [8] did so for the characterization of fluid flows by a map of vortex and source particles, whereas we use it for separate regularization of the the irrotational and solenoidal parts of the flow field based on covariant derivatives and gauge fields. Furthermore, our algorithm aims at tracking cardiac motion, whereas Cuzol et al. applied their method to meteorological data, airplane wings, and brain data. Based on [4], Mansi et al. proposed a nonrigid registration algorithm incorporating tissue incompressibility, and applied it to cardiac 3D cardiac MR tagging and cardiac

O. Camara et al. (Eds.): STACOM 2011, LNCS 7085, pp. 263–273, 2012.

cine MRI [9]. An incompressibility constraint is not desired in our approach, as in 2D incompressibility does not apply, and due to through-plane motion. Furthermore, during systole myocardial volume is reduced by approximately 8%, because blood is squeezed out.

Many optic flow methods are based on the brightness constancy assumption without taking into account the physical properties of the data. The motivation to embed the Helmholtz decomposition in our method is the fact that the cardiac motion consists of a combination of rotation and contraction. Such a combination can be well characterized by div-curl regularizers. Moreover, from a clinical point of view, solenoidal and irrotational parts of the vector field may be analyzed independently to reveal and quantify abnormal deformation in the tissue. The novelty of our contribution is threefold:

(i) we propose a multi-scale variational feature tracking and dense flow field reconstruction method for MRI tagging;
(ii) we separate motion into *independently regularized* solenoidal and irrotational components using Helmholtz decomposition [10];
(iii) we extend standard Tikhonov regularization by incorporating *covariant derivatives* biased by a "gauge field".

Performance is assessed quantitatively on two phantoms, and on MRI tagging data obtained from a healthy volunteer and a patient with myocardial infarcts. For a schematic overview of our method, see Fig. 1.

2 Multi-scale Feature-Based Tracking Using Optical Flow

2.1 Image Data Set and Preprocessing

MR tags are artificial periodic intensity patterns, obtained by spatial modulation of magnetization (SPAMM) [11], cf. Fig. 2(a). Current methods for analysing MRI tagging images are optical flow [12,13], finite element models [14], nonrigid

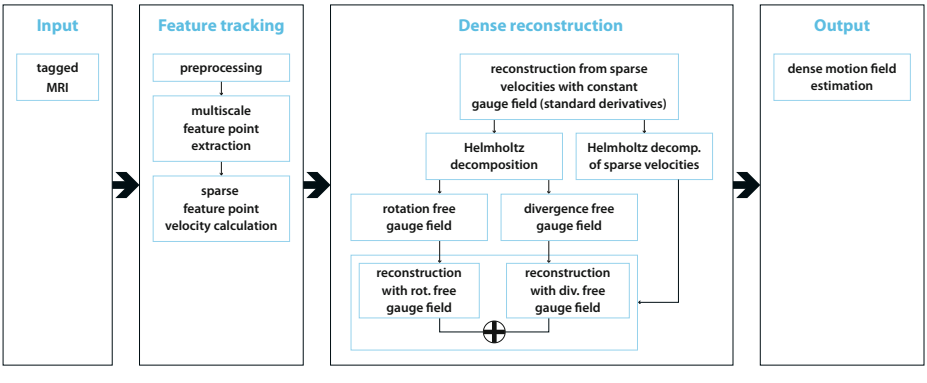

Fig. 1. Schematic overview of our method

registration [15], stripe following [16,17], and Fourier methods, such as (3D) HARP [18,19], sine wave modeling [20], and Gabor filtering [21]. The constant brightness assumption underlying some techniques is not applicable to MRI tagging due to T_1 relaxation (causing tag fading). Other methods are limited in that they are based on sparse landmark sets degrading resolution. For a review of MRI motion analysis protocols, see [22].

We extract discontinuity-free sine phase images using Gabor filters [23], cf. Fig. 2(b). Horizontal and vertical tags are combined into a grid, cf. Fig. 2(c).

2.2 Calculation of Sparse Velocity Features

At a critical point the spatial gradient—obtained using Gaussian derivatives at scale $s>0$—vanishes, $\nabla I(\mathbf{x}, s, t) = 0$. From this one can infer subpixel estimates of its position $\mathbf{x}$ at time t as a function of scale s [24]. A label $q = 1, \ldots, N_B$ identifies a critical point. Given s, tracking relies on the implicit constraint

$$\nabla I(\mathbf{x}_s^q(t), s, t) = 0\,, \tag{1}$$

in which $I(\mathbf{x}_s^q(t), s, t)$ represents the intensity at $\mathbf{x}_s^q(t) = \mathbf{x}_s^q(0) + \int_0^t \dot{\mathbf{x}}_s^q(\tau)d\tau$. By partitioning the time interval $[0, T]$ into discrete intervals labeled by t_k, with $k = 1, \ldots, K$, $t_0 = 0$, $t_K = T$, this yields a sparse set of velocities $\widetilde{\mathbf{v}}(\mathbf{x}_s^q(t_k)) = \dot{\mathbf{x}}_s^q(t_k) = \mathbf{v}(\mathbf{x}_s^q(t_k), t_k)$. Differentiation of (1) with respect to t yields [24]

$$\widetilde{\mathbf{v}}(\mathbf{x}_s^q(t_k)) = \begin{bmatrix}\widetilde{u}(\mathbf{x}_s^q(t))\\ \widetilde{v}(\mathbf{x}_s^q(t))\end{bmatrix} = \begin{bmatrix}u(\mathbf{x}_s^q(t), t)\\ v(\mathbf{x}_s^q(t), t)\end{bmatrix} = -(H(\mathbf{x}_s^q, s, t))^{-1}\frac{\partial(\nabla I(\mathbf{x}_s^q, s, t))}{\partial t} \tag{2}$$

where H represents the spatial Hessian matrix of image I. In the remainder of this article we will denote the velocity vectors at the critical points as

$$\mathbf{d}_q^k := \begin{pmatrix} d_q^{k,1}\\ d_q^{k,2}\end{pmatrix} := \begin{pmatrix}\widetilde{u}(\mathbf{x}_s^q(t_k))\\ \widetilde{v}(\mathbf{x}_s^q(t_k))\end{pmatrix}\,. \tag{3}$$

Velocities are necessarily retrieved at a certain scale. The most appropriate scale may vary from point to point. The slope of the tangent vector along a critical path $s \mapsto (\mathbf{x}_s^q(t), s)$ in scale space (t fixed) provides a measure for its spatial stability. Hence for each critical path q at fixed time $t \geq 0$ we choose the highest scale s_q such that the slope of the tangent vector along the critical path is below a certain a priori angle ϑ with respect to the scale direction [24].

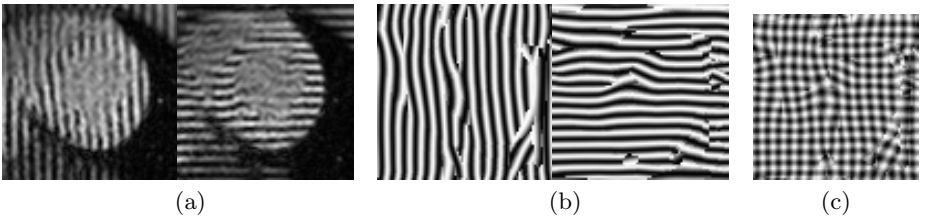

(a) (b) (c)

Fig. 2. (a) Tagged short axis views of a left ventricle. (b) Sine-phase images. (c) Sum of sine-phase images. Images are 80×80 pixels with pixel size of 1.36×1.36 mm^2.

3 Vector Field Decomposition

The cardiac muscle exhibits twistings and contractions, suggesting a Helmholtz decomposition [10]. Given a bounded domain $\Omega \subseteq \mathbb{R}^3$ and a vector field $\mathbf{v} \in \mathbf{C}^0(\overline{\Omega}) \bigcap \mathbf{C}^1(\Omega)$, functions $\Phi, \mathbf{A} \in \mathbf{C}^1(\overline{\Omega})$ exist such that

$$\mathbf{v} = \nabla\Phi + \nabla \times \mathbf{A} \quad \text{and} \quad \nabla \cdot \mathbf{A} = 0\,. \tag{4}$$

The functions Φ and $\mathbf{A}$ are the so-called *scalar potential* and *vector potential*, and $\nabla\Phi$ and $\nabla \times \mathbf{A}$ represent the *irrotational* and *solenoidal* components of $\mathbf{v}$. However in our cardiac MRI tagging application we consider $\Omega \subset \mathbb{R}^2$, and in $\mathbb{R}^2$ one does not have an outer product. We therefore need the following definition.

Definition 1. *In terms of Euclidean coordinates we define the rotation of a 2D-vector vector field and of a 2D-scalar field, respectively, as*

$$\operatorname{rot} \mathbf{v} = \partial_x v^2 - \partial_y v^1 \quad \textit{resp.} \quad \widetilde{\operatorname{rot}}\, f = \begin{pmatrix} \partial_y f \\ -\partial_x f \end{pmatrix}. \tag{5}$$

3D Helmholtz decomposition is extended to 2D by applying (5) consistently. To obtain explicit formulas, we approximate[1] a solution to the Poisson equation [25] on Ω:

$$\Delta\boldsymbol{\xi} = \mathbf{v} \tag{6}$$

viz.

$$\boldsymbol{\xi}(\mathbf{x}) = \int_{\Omega} G^{2D}(\mathbf{x} - \mathbf{x}')\mathbf{v}(\mathbf{x}')\mathrm{d}\mathbf{x}' \tag{7}$$

where

$$G^{2D}(\mathbf{x} - \mathbf{x}') = \frac{1}{2\pi} \ln \|(\mathbf{x} - \mathbf{x}')\| \ . \tag{8}$$

is the so-called Green's function of the two-variables Poisson equation. Moreover, $\boldsymbol{\xi}$ satisfies $\Delta\boldsymbol{\xi} = \nabla(\nabla \cdot \boldsymbol{\xi}) - \widetilde{\operatorname{rot}}\,(\operatorname{rot} \boldsymbol{\xi})$. From this and (6) we obtain

$$\mathbf{v} = \nabla\Phi + \widetilde{\operatorname{rot}}\, A\,, \tag{9}$$

cf. (4), with $\Phi = \nabla \cdot \boldsymbol{\xi}$ and $A = -\operatorname{rot} \boldsymbol{\xi}$. However, this decomposition is not unique. The decomposition is unique if we subtract the harmonic infilling $\boldsymbol{\psi}$ from the original vector field [26]. Hence

$$\widetilde{\mathbf{v}} = \mathbf{v} - \boldsymbol{\psi} \tag{10}$$

vanishes at the boundaries. Our aim is a dense reconstruction of $\widetilde{\mathbf{v}}$ and its unique Helmholtz decomposition from the sparse evidence represented by (3).

[1] If $\Omega = \mathbb{R}^2$ it is an exact solution.

3.1 Multi-scale Helmholtz Decomposition of the Optical Flow Field

Instead of using standard derivatives in (7–10), the Green's function can be differentiated by convolution with derivatives of a Gaussian kernel. This introduces a scale parameter $s = \frac{1}{2}\sigma^2$, and simultaneously removes the singularity at the origin. The first order Gaussian derivatives of the Green's function are:

$$\partial_{x^i} G_s^{2D}(\mathbf{x}) = \frac{1}{2\pi} \frac{x^i \left(1 - \exp(-\frac{x^2+y^2}{4s})\right)}{x^2+y^2} \,. \tag{11}$$

By combining (7–10) and (11) one obtains

$$\tilde{\mathbf{v}}_s := \text{grad}\,(\partial_{x^1} G_s^{2D} * \tilde{v}^1 + \partial_{x^2} G_s^{2D} * \tilde{v}^2) - \widetilde{\text{rot}}\,(-\partial_{x^2} G_s^{2D} * \tilde{v}^1 + \partial_{x^1} G_s^{2D} * \tilde{v}^2) \tag{12}$$

where $*$ denotes convolution. We note that the effective kernel operators can be pre-computed *analytically* [26]. The original vector field (at scale s) is given by

$$\mathbf{v}_s = \widetilde{\mathbf{v}}_s + \boldsymbol{\psi} \,. \tag{13}$$

3.2 Experiments on the Decomposition of the Vector Field

To assess the accuracy of the irrotational and solenoidal components, and of the recomposed vector field (12–13), a ground-truth phantom was created for a multi-scale Helmholtz decomposition (Fig. 3 top row)

$$\mathbf{v}_s := G_s * \mathbf{v}_0 = -2\gamma \begin{pmatrix} \partial_x \phi_{s+\gamma} \\ \partial_y \phi_{s+\gamma} \end{pmatrix} - 2\gamma \begin{pmatrix} -\partial_y \phi_{s+\gamma} \\ \partial_x \phi_{s+\gamma} \end{pmatrix}, \tag{14}$$

with $(x, y) \in [-1, 1] \times [-1, 1]$, $s > 0$, $\gamma = 0.02$ fixed, where ϕ_s denotes the Gaussian kernel. Computations were performed at scale $s = 1$ on a uniform 101×101 grid with spatial step size 0.02, and evaluated using the average angular error (AAE) [27]. Comparing the recomposed vector field $\mathbf{v}_{s=1}$ to the original vector field $\mathbf{v}_0$ yields AAE $= 0.40°$, confirming the visual similarity of the original and recomposed vector fields (see Fig. 3). Comparing $\mathbf{v}_{s=1}$ numerically computed using the exact effective kernels [26, Thm 4.4] to the true $\mathbf{v}_{s=1}$ vector field at the same scale, yields negligible angular error (AEE $= 0.0043°$).

3.3 Covariant Derivatives and Reconstruction

The covariant derivative of a function $f : \Omega \to \mathbb{R}$ with respect to an a priori *gauge function* $h : \Omega \to \mathbb{R}$ is defined as

$$D_{x^i}^h f(x, y) = \partial_{x^i} f(x, y) - \frac{\partial_{x^i} h(x, y)}{h(x, y)} f(x, y) \tag{15}$$

where $(x^1, x^2) = (x, y) \in \Omega \subset \mathbb{R}^2$ and $h(x, y) \neq 0$. Tikhonov regularization by regular derivatives ($h(x, y) =$ constant) suffers from the drawback that at areas where only few features are present the solution tends towards a constant.

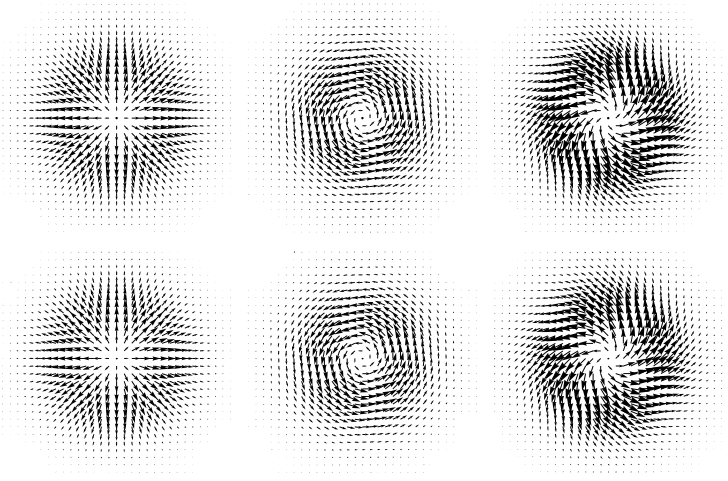

Fig. 3. Top row: ground truth Helmholtz decomposition of the phantom field $\mathbf{v}_{s=0}$, cf. (14). Bottom row: output $\mathbf{v}_{s=1}$ of the Helmholtz decomposition algorithm, cf. (13). Left to right: divergence free, rotation free, full field.

The use of covariant derivatives drives the solution towards the a priori gauge function instead ("background field"). We construct the gauge function as the solution of a sparse velocity reconstruction using Tikhonov regularization with *standard derivatives*, and subsequently refine the reconstruction using *covariant derivatives* instead. The refinement is less biased towards constant velocities and moreover it employs the features *twice*, both in the data- and regularization term. For details, cf. [26].

3.4 Feature Based Optic Flow Equation with Covariant Derivatives and Helmholtz Decomposition (CDHD)

We aim to retrieve $\mathbf{v}^k$ at time-step k, by minimizing the energy functional

$$\mathcal{E}^{\lambda,\mathbf{h}^k,\mathbf{d}^k}(\mathbf{v}^k) = \mathcal{E}^{\mathbf{h}^k}_{\text{reg}}(\mathbf{v}^k) + \mathcal{E}^{\mathbf{d}^k}_{\text{data}}(\mathbf{v}^k) = \sum_{q=1}^{N_B} w_q^k \sum_{j=1}^{2} |(\phi_{s_q} * v^{k,j})(\mathbf{x}_q) - d_q^{k,j}|^2 + \lambda \int_\Omega \sum_{i=1}^{2}\sum_{j=1}^{2} |D_{x^i}^{h^{k,j}} v^{k,j}(\mathbf{x})|^2 \, \mathrm{d}\mathbf{x} \tag{16}$$

where $w_q^k \in \mathbb{R}^+$ is a weight factor, $\lambda > 0$ provides balance between regularization and the data term, q enumerates the extremal branches. Index $j \in \{1, 2\}$ indicates the vertical and horizontal component of the field and $x^i \in \{x, y\}$. Moreover, $\phi_k^q(\mathbf{x}) := \phi_{s_q}(\mathbf{x} - \mathbf{x}_q)$ denotes the Gaussian kernel centered around $\mathbf{x}_q$ with scale $s_q > 0$ and the sparse velocity components $d_q^{k,j}$ in (3) are derived by solving (2). Minimization of (16) was carried out by exact solutions of the discrete Euler Lagrange equations [26].

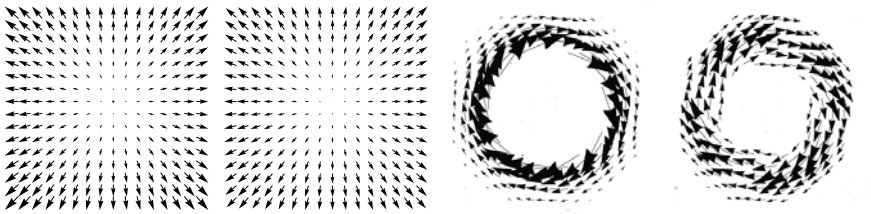

Fig. 4. Phantom 1 frame 5: ground truth (a), reconstructed vector field (b). Phantom 2 frame 3: ground truth (c) and reconstructed vector field (d). Arrows are magnified.

To reconstruct the rotation-free and divergence-free components of a vector field separately, we include the multi-scale Helmholtz decomposition in (16). To this end we also decompose the sparse velocities into divergence-free and rotation-free components: $\mathbf{d}^k = \mathbf{d}^k_{df} + \mathbf{d}^k_{rf}$. Namely, we reconstruct the velocity field by a regularization with standard derivatives at very small $0 < \lambda \ll 1$, to obtain a regularized velocity field that (nearly) satisfies the hard constraints (as $0 < \lambda \ll 1$). Then we apply a multi-scale Helmholtz decomposition on this field and we extract its divergence-free and rotation-free parts at the position $\mathbf{x}_q$ and scale s_q of interest (we use pre-computed exact analytic kernels [26, Thm 4.4]).

Hence, to calculate a dense motion field, we minimize (16) separately over solenoidal (df) and irrotational (rf) parts,

$$\mathbf{v}^k = \underset{\mathbf{v}}{\operatorname{argmin}}\ \mathcal{E}^{\lambda_1,\mathbf{h}^k_{\mathrm{rf}},\mathbf{d}^k_{\mathrm{rf}}}(\mathbf{v}) + \underset{\mathbf{w}}{\operatorname{argmin}}\ \mathcal{E}^{\lambda_2,\mathbf{h}^k_{\mathrm{df}},\mathbf{d}^k_{\mathrm{df}}}(\mathbf{w}). \tag{17}$$

4 Experiments and Results

Our method was evaluated on two different ground truth phantoms. Phantom 1 consists of 19 time-frames (99×99 pixels) of an irrotational pattern (Fig. 4(a)). Phantom 2 [28] has 13 frames (93×93 pixels) and shows non-rigid rotation (Fig. 4(c)). The analytic function for phantom 1 is $v^i(x,y,t) = \frac{(x^i - l)(m - 2n\cdot t)}{(l + (m - n\cdot t)t}$, $l = 50$, $m = 5$, and $n = 0.25$. In both phantoms the motion vanishes at the boundaries. We index our parameters as follows. The smoothness in the dense flow field reconstruction is controlled by λ_1, and η_1 denotes the interpolation parameter between covariant and standard derivatives, both of the rotation-free part. The parameters for the divergence-free part are λ_2 and η_2. Parameter η governs the influence of the covariant derivative by taking the η (sign-preserving) power of the gauge function; $D^{h^\eta} f = \partial_{x^i} f - \eta \cdot \frac{\partial_{x^i} h}{h} f$.

Increasing $\lambda \in \{10^{-2}, 10^{-1}, 1, 10, 100, 10^3, 10^4, 10^5, 10^6\}$ increases the smoothness of the reconstructed motion field. We choose λ such that the AAE and the L2 norm error w.r.t. the ground truth is minimized.

Table 1. Performance of our method using different reconstructions on phantom 1

Reconstruction Methodology ↓	AAE	L2 Norm	parameter
Conventional Derivatives	$1.26° \pm 1.11°$	$4.2 \times 10^{-2} \pm 0.04$	$\lambda = 10^{-2}$
Covariant Derivatives	$1.20° \pm 1.01°$	$3.6 \times 10^{-2} \pm 0.03$	$\lambda = 10^2$, $\eta = 0.7$
Covariant Derivatives and Helmholtz Decomposition	$0.97° \pm 0.62°$	$3.3 \times 10^{-2} \pm 0.03$	$\lambda_1 = 10^{-2}$, $\lambda_2 = 10^2$ $\eta_1 = 0.9$, $\eta_2 = 0.5$

Table 2. Performance of our method using different reconstructions on phantom 2

Reconstruction Methodology ↓	AAE	L2 Norm	parameter
Conventional Derivatives	$8.05° \pm 9.09°$	0.21 ± 0.26	$\lambda = 1$
Covariant Derivatives	$7.30° \pm 9.81°$	0.19 ± 0.25	$\lambda = 10$, $\eta = 0.9$
Covariant Derivatives and Helmholtz Decomposition	$6.68° \pm 9.48°$	0.16 ± 0.24	$\lambda_1 = 10^2$, $\lambda_2 = 10^3$ $\eta_1 = 0.5$, $\eta_2 = 0.7$

Table 3. Performance comparison with other optic flow methods on phantom 2

Method ↓	AAE	L2 Norm	parameter
Horn & Schunck [1]	$5.78°$	0.16	$\lambda = 0.5$
Lucas & Kanade [2]	$5.08°$	0.22	$\lambda = 0.01$
Conventional Derivatives	$5.33°$	0.14	$\lambda = 1$
Covariant Derivatives and Helmholtz Decomposition	$3.84°$	0.11	$\lambda_1 = 10^2$, $\lambda_2 = 10^3$ $\eta_1 = 0.5$, $\eta_2 = 0.9$

When reconstructing based on CDHD, λ_2 and λ_1 were fixed for phantoms 1 and 2 respectively and the other λ component was optimized. Once the λ_i parameter is tuned, parameter $\eta_i \in \{0.5, 0.7, 0.9, 1., 1.1, 1.3\}$, $i = 1, 2$ is investigated, which governs the influence of the gauge field in the velocity field reconstruction. The outcome of the optic flow method based on conventional derivatives of time frame k is used as the gauge field to reconstruct the motion field at time k. This is only one of the possible gauge field choices. For the reconstruction based on CDHD, η_2 and η_1 are fixed for phantoms 1 and 2 respectively. The other η_i are selected such that the AAE is minimized (see Tables 1, 2, 3).

The error measurements during algorithm evaluation are an average over three subsequent frames. Tables 1 and 2 show the performance of our optic flow method, using multi-scale maxima as feature points only, based on the AAE and the L2 norm, comparing standard derivatives, covariant derivatives, and CDHD respectively. For both phantoms, one frame of the retrieved motion fields together with their ground truths is shown in Fig. 4. Table 3 shows a comparison of our methods with Horn & Schunk [1] and Lucas & Kanade [2] on phantom 2. For a fair comparison, we included more features (maxima, minima and saddle points) in our method to get a less sparse set of velocity vectors $\mathbf{d}_q^k$ before dense field reconstruction. This led to a slightly different optimal value for η_2 for CDHD. For the Horn & Schunk method, $\lambda \in \{0.05, 0.5, 5, 50, 500\}$ was also optimized for best performance. In our implementation of the Lucas and Kanade algorithm, the eigenvalues of the motion matrix were thresholded, using $\lambda \in \{0.1, 0.05, 0.01, 0.005, 0.001\}$ as the threshold, which was optimized (Tab. 3).

We compared the motion fields extracted from a healthy volunteer and a patient, who suffered a number of small infarctions. Systolic tagged MR images

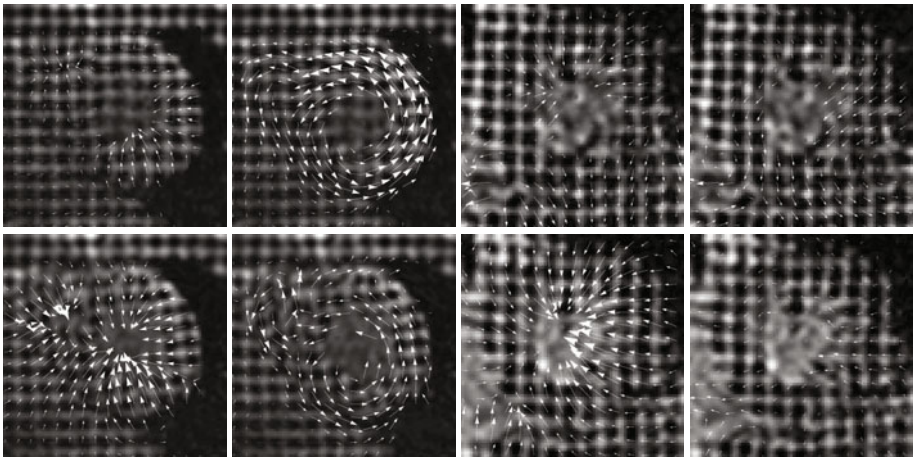

Fig. 5. Rotation-free (a,c) and divergence-free (b,d) parts of true cardiac motion fields for a healthy volunteer (a,b) and the patient (c,d), frames 3 (top) and 6 (bottom). Note that the patient lacks rotational motion (div-free part) in both frames, whereas the rotation-free part is affected locally.

were acquired; 11 frames, pixel size of $1.2 \times 1.2mm^2$, slice thickness of $8mm$. In Fig. 5 the rotation-free (a,c) and divergence-free (b,d) parts of boths hearts are shown. At early systole, the healthy heart shows little contraction and a strong rotation (Fig. 5(a,b), top). Later, the contribution of both parts becomes comparable (Fig. 5(a,b), bottom). The infarcted heart lacks rotation in both frames (Fig. 5(d)), leaving contraction only (Fig. 5(c)).

5 Discussion and Conclusion

Multi-scale Helmholtz decomposition allows assessment of irrotational and solenoidal motion separately. We have shown that extending Tikhonov regularization by incorporating a gauge field based on multi-scale covariant derivatives improves dense motion field reconstruction. The proposed approach outperforms similar techniques that use regular derivatives and without Helmholtz decomposition, and outperforms other optic flow methods. The influence of noise is reduced by scale selection based on the slope of the tangent vector along each critical path in scale space [24], thus providing also a measure for spatial stability of each critical point. Furthermore, the Gabor filters remove the influence of noise outside their frequency band. Inclusion of more features than maxima only improves motion field reconstruction. Application to tagged MR images showed its potential for diagnostics. Currently, we are evaluating our technique on a large population.

References

1. Horn, B.K.P., Shunck, B.G.: Determining optical flow. AI 17, 185–203 (1981)
2. Lucas, B., Kanade, T.: An iterative image registration technique with application to stereo vision. In: DARPA, Image Process, vol. 21, pp. 85–117 (1981)
3. Florack, L., van Assen, H.: Dense multiscale motion extraction from cardiac cine MR tagging using HARP technology. In: ICCV Workshop on MMBIA (2007)
4. Thirion, J.: Image matching as a diffusion process: an analogy with Maxwell's demons. Med. Imag. Anal. 2(3), 243–260 (1998)
5. Janssen, B., Florack, L., Duits, R., ter Haar Romeny, B.: Optic Flow from Multiscale Dynamic Anchor Point Attributes. In: Campilho, A., Kamel, M.S. (eds.) ICIAR 2006. LNCS, vol. 4141, pp. 767–779. Springer, Heidelberg (2006)
6. Kohlberger, T., Mémin, E., Schnörr, C.: Variational Dense Motion Estimation Using the Helmholtz Decomposition. In: Griffin, L.D., Lillholm, M. (eds.) Scale-Space 2003. LNCS, vol. 2695, pp. 432–448. Springer, Heidelberg (2003)
7. Corpetti, T., Mémin, E., Pérez, P.: Dense estimation of fluid flows. IEEE Trans. Pattern Anal. Mach. Intell. 24(3), 365–380 (2002)
8. Cuzol, A., Hellier, P., Mémin, E.: A low dimensional fluid motion estimator. IJCV 75, 329–349 (2007), doi:10.1007/s11263-007-0037-0
9. Mansi, T., Pennec, X., Sermesant, M., Delingette, H., Ayache, N.: iLogDemons: A demons-based registration algorithm for tracking incompressible elastic biological tissues. IJCV 92(1), 92–111 (2011)
10. von Helmholtz, H.: Üeber integrale der hydrodynamischen Gleichungen, welche den Wirbelbewegungen entsprechen. Crelles J. 55(25) (1858)
11. Axel, L., Dougherty, L.: MR imaging of motion with spatial modulation of magnetization. Radiology 171(3), 841–845 (1989)
12. Prince, J.L., McVeigh, E.R.: Motion estimation from tagged MR image sequences. IEEE Trans. Med. Imaging 11(2), 238–249 (1992)
13. Gupta, S.N., Prince, J.L.: On Variable Brightness Optical Flow for Tagged MRI. In: Proc. of 14th Int. Conf., IPMI 1995. Kluwer, Dordrecht (1995)
14. Young, A.A.: Model tags: direct three–dimensional tracking of heart wall motion from tagged magnetic resonance images. Med. Image Anal. 3(4), 361–372 (1999)
15. Chandrashekara, R., Mohiaddin, R., Rueckert, D.: Analysis of myocardial motion in tagged mr images using nonrigid image registration. In: Proc. of SPIE, vol. 4684, pp. 1168–1179 (2002)
16. Amini, A., Chen, Y., Elayyadi, M., Radeva, P.: Tag surface reconstruction and tracking of myocardial beads from spamm-mri with parametric b-spline surfaces. IEEE Trans. Med. Imaging 20(2), 94–103 (2001)
17. Axel, L., Chen, T., Manglik, T.: Dense Myocardium Deformation Estimation for 2D Tagged MRI. In: Frangi, A.F., Radeva, P., Santos, A., Hernandez, M. (eds.) FIMH 2005. LNCS, vol. 3504, pp. 446–456. Springer, Heidelberg (2005)
18. Osman, N.F., Kerwin, W.S., McVeigh, E.R., Prince, J.L.: Cardiac motion tracking using CINE harmonic phase (HARP). Magnetic Resonance Imaging, MRM 42(6), 1048–1060 (1999)
19. Pan, L., Prince, J.L., Lima, J.A.C., Osman, N.F.: Fast tracking of cardiac motion using 3D–HARP. IEEE Trans. Biomed. Eng. 52(8), 1425–1435 (2005)
20. Arts, T., Prinzen, F.W., Delhaas, T., Milles, J.R., Rossi, A.C., Clarysse, P.: Mapping displacement and deformation of the heart with local sine-wave modeling. IEEE Trans. Med. Imaging 29(5), 1114–1123 (2010)

21. Chen, T., Wang, X., Chung, S., Metaxas, D., Axel, L.: Automated 3d motion tracking using gabor filter bank, robust point matching, and deformable models. IEEE Trans. Med. Imaging 29(1), 1–11 (2010)
22. Ozturk, C., Derbyshire, J.A., McVeigh, E.R.: Estimating motion from MRI data. Proc. of the IEEE 91(10), 1627–1648 (2003)
23. Gabor, D.: Theory of communication. J. IEE 93(26), 429–457 (1946)
24. Florack, L., Kuijper, A.: The topological structure of scale-space images. JMIV 12(1), 65–79 (2000)
25. Dassios, G., Lindell, I.: Uniqueness and reconstruction for the anisotropic Helmholtz decomposition. J. Phys. Math. Gen. 35, 5139–5146 (2002)
26. Duits, R., Janssen, B.J., Becciu, A., van Assen, H.C.: A variational approach to cardiac motion estimation based on covariant derivatives and multi-scale helmholtz decomposition. Quarterly of Applied Mathematics (accepted)
27. Barron, J., Fleet, D., Beauchemin, S.: Performance of optical flow techniques. IJCV 12(1), 43–77 (1994)
28. Young, A.A., Axel, L., Dougherty, L., Bogen, D.K., Parenteau, C.S.: Validation of tagging with mr imaging to estimate material deformation. Radiology 188(1), 101–108 (1993)